

# Numerical investigation of heat and mass transfer of variable viscosity Casson nanofluid flow through a microchannel filled with a porous medium

Lemi Guta Enyadene, Ebba Hindebu Rikitu\*, Adugna Fita Gabissa

Department of Applied Mathematics, Adama Science and Technology University, Adama 1888, Ethiopia

\* Corresponding author: Ebba Hindebu Rikitu, ebba.hindebu@astu.edu.et

## ARTICLE INFO

Received: 2 July 2023  
Accepted: 9 August 2023  
Available online: 7 September 2023

doi: 10.59400/jam.v1i3.194

Copyright © 2023 Author(s).

*Journal of AppliedMath* is published by Academic Publishing Pte. Ltd. This article is licensed under the Creative Commons Attribution License (CC BY 4.0).  
<https://creativecommons.org/licenses/by/4.0/>

**ABSTRACT:** Thermal behaviours and hydrodynamics of non-Newtonian nanofluids flow through permeable microchannels have large scale utilizations in industries, engineering, and biomedicine. Therefore, this paper presents the numerical investigation of heat and mass transfer of variable-viscosity Casson nanofluid flow through a porous medium microchannel with the Cattaneo-Christov heat flux theory. The highly nonlinear PDEs corresponding to the continuity, momentum, energy, and concentration equations are formulated and solved numerically via the second-order implicit finite difference scheme known as the Keller-Box method. Accordingly, the numerical simulations reveal that the variable viscosity parameter, thermal Grashof number, solutal Grashof number, thermophoresis parameter, Schmidt number, and Casson fluid parameter show increasing effects on both velocity and temperature of the nanofluid. Furthermore, the temperature profile escalates with increasing values of the Eckert number and the thermal relaxation time parameter. Thus, the Cattaneo-Christov heat flux model is beneficial in warming the transport system of microfluidics when compared to that of the classical Fourier heat conduction law. The temperature profile, however, indicates a retarding behavior with increasing values of the Brownian motion parameter, Prandtl number, and porous medium parameters, namely the Forchheimer number and porous medium shape parameter, and hence, the porous medium quite effectively controls the nanofluid temperature distribution, which plays substantial roles in cooling the transport system of microfluidics. Moreover, the concentration profile shows an increasing pattern with escalating values of the Prandtl number, Schmidt number, and thermophoresis parameter, but it demonstrates a decreasing trend with the Casson fluid, variable viscosity, thermal relaxation time, and solutal relaxation time parameters. It is also observed that the coefficient of skin friction increases with increasing values of the pressure gradient parameter, Eckert number, Forchheimer number, and injection/suction Reynolds number. Besides, the heat transfer rate at both walls of the microchannel increases with rising values of the Eckert number, variable viscosity, parameter, and injection/suction Reynolds number. The Casson fluid and thermal relaxation time parameters reveal opposite scenarios for the heat transfer rate at the left and right walls of the microchannel. In addition

the mass transfer rate at both walls of the microchannel shows an increasing pattern as the Eckert number, variable viscosity parameter, Schmidt number, and suction/injection Reynolds number increase.

**KEYWORDS:** microchannel; Casson fluid; porous media; variable viscosity; thermal relaxation time; solutal relaxation time

---

## 1. Introduction

Nowadays, with increasing energy prices and a demand for energy efficiency, many efforts are made for energy savings and reduction of production costs, and hence augmentation of convective heat as well as energy storage are the charming issues in engineering associated with energy conservation<sup>[1]</sup>. Consequently, during the past decades, numerous techniques were devised to advance the performance of industrial equipment, particularly in various heat energy-transforming devices or heat exchangers. This scientific revolution ensured strong industrial productivity growth, which in turn has improved societal quality of life worldwide. In general, the goal is to improve the thermal efficiency of heat conversion devices, which is referred to as heat transfer rate augmentation, which improves the overall performance of the industrial system, including reducing the initial and capital costs of the heat transfer devices or heat exchangers.

For internal flows such as fluids flowing in tubes or channels, the convective rate of heat transfer can be augmented through techniques that do not require additional external power, such as refinement of flow channel geometry and fluid additives<sup>[2]</sup>. As far as channel geometry refinement is concerned, microchannels have been identified as the most essential ones to transport fluids in a miniaturization system. To this end, in 1981, the concept of microchannels was predominantly demonstrated by Tuckerman and Pease<sup>[3]</sup> who achieved a high heat flux removal capacity of about  $800 \text{ W/cm}^2$  within heat exchangers by utilizing a channel with a hydraulic diameter of  $100 \mu\text{m}$ . Microchannels are increasingly used in several industrial and engineering applications that span from the cooling of microelectronics to bio-technological applications<sup>[4]</sup>. Therefore, there are numerous research studies that are reporting investigations of various fluid flows through microchannels. For example, the combined effects of viscous-Joule dissipation and slip wall on the electro-osmotic peristaltic flow of the Casson fluid in a rotating microchannel are investigated by Reddy et al.<sup>[5]</sup>. Later on, Kmiotek and Kucab-Pietal<sup>[6]</sup> presented the study of heat transfer phenomena in a microchannel in the presence of slender porous material.

Although they are well known for their great heat-removal capacities, fluid flows through microchannels encounter excessive pressure drop, which thus involves great pumping power<sup>[7]</sup>. In addition, conventional base fluids like water, ethylene-glycol, and oils are poor in heat transfer capacities because of their low thermal conductivity<sup>[8]</sup>. Due to these facts, new technological fluids with enhanced thermophysical properties such as thermal conductivity and dynamic viscosity are of prodigious interest for microchannel flows. In this regard, the insertion of nanometer-sized ( $1 \text{ nm} = 1 \times 10^{-9} \text{ m}$ ) solid particles into conventional fluids is one of the most fruitful convective heat transfer enhancement methods. Thus, with persistent diminishment as well as growing heat elimination in novel brands of devices, there is a need for the most effective heat transfer fluids in microchannels. In 1995, Choi and Eastman<sup>[9]</sup> were the first scientists to introduce the idea of nanofluids, meaning nanofluids are engineered suspensions or dispersions of nanoparticles into common base fluids. Since then, nanofluid flows through microchannels have been utilized in the cooling of various technological

and industrial processes<sup>[10]</sup>. Therefore, numerous researchers, including<sup>[11–18]</sup> are working on the analysis of nanofluid flow as well as heat transfer characteristics through microchannels.

The rates of heat transfer through microchannels become enhanced through the amalgamation of nanofluids and porous media. Actually, the convective flows in porous media have significant applications, including the extraction of crude oil, the extraction of geothermal energy, pollution of groundwater, radioactive nuclear waste storage, cooling in transpiration, filtration in chemical industries, purification, transportation processes in aquifers, and fiber insulation<sup>[19,20]</sup>. Consequently, nowadays, the analysis of thermal behaviors and flow of nanofluids through porous media has received a great deal of attention. For example, Algehyne et al.<sup>[21]</sup> studied the hydrodynamics of chemically reacting water based alumina nanoparticles past over a curved porous geometry under multiple convective constraints by adopting the Buongiorno's and Koo-Kleinstreuer-Li's nanofluid models. The nonlinear governing equations were numerically tackled by employing the irregular generalized differential quadrature scheme together with the Newton-Raphson method. Their outcomes indicated that the nanofluid velocity decreased as the slip-velocity and drag forces escalated. Also, Rashad et al.<sup>[22]</sup> investigated the partial slip and MHD combined convective flow of Cu-water nanofluid and heat transfer characteristics inside a lid-driven porous enclosure.

Maneengam et al.<sup>[23]</sup> numerically investigated the influences of Lorentz and Buoyancy forces on the hybrid fluid comprising  $\text{Al}_2\text{O}_3$ -Cu nanoparticles through a lid-driven container having obstacles of various shapes. The numerical simulation was given via the Galerkin finite element method, and it was observed that the triangular shape of the obstacle enhanced the thermal performance. That is, the Nusselt number increased by 15.54% when the baffle altered its shape from the elliptic to the triangular. Moreover, the electro-magneto-hydrodynamic investigation of nanofluid motion over a Riga plate filled with a Darcy-Forchheimer porous medium was presented by Rasool et al.<sup>[24]</sup>. The governing partial differential equations were transformed into ordinary differential equations by using appropriate similarity variables and thereafter tackled numerically. Thus, nanofluid velocity is remarkably influenced by the Darcy-Forchheimer porous medium. In addition, the Darcy-Forchheimer and Lorentz forces enhanced the skin friction coefficient. Furthermore, Makinde et al.<sup>[25]</sup> presented the numerical investigation of steady hydromagnetic nanofluid convection inside the micro-porous channel with injection/suction, radiative heat, and heat absorption/generation. Besides, to read more on heat transfer phenomena as well as the motion of fluids through porous media, the references<sup>[26–30]</sup> are preferable.

The Casson fluid model can be regarded as the most appropriate for industrial applications, for instance, exploring the mechanism of pseudoplastic yield stress liquids in food processing, metallurgy, drilling, and bio-engineering operations<sup>[31]</sup>. Therefore, nowadays, a reasonable number of communications can be quoted highlighting the Casson fluid model in the existing literature. For instance, Thammanna et al.<sup>[32]</sup> presented the transient analysis of the magnetohydrodynamic stretched flow of a couple-stress Casson fluid with a chemical reaction. Similarly, Mahanthesh et al.<sup>[33]</sup> addressed the boundary layer flow and heat transfer in Casson fluid submerged with dust particles over three different geometries (vertical cone, wedge, and plate). The governing equations were solved by the shooting method coupled with the Runge-Kutta-Fehlberg-45 integration scheme. According to their results, a rise in the Casson fluid parameter enhances the fluid temperature, and the magnetic field improves heat transfer rate. Besides, very recent papers like references<sup>[34,35]</sup> comprise similar Casson fluid analyses.

The above literature review can establish that the analysis of various nanofluid flow as well as heat and mass transfer phenomena through microchannels because of free or forced convection was presented in detail. However, limited studies on mixed convection as well as heat and mass transfer characteristics of Casson fluid through a vertical microchannel embedded with a saturated porous medium have been carried out. Even those investigations are rare in considering temperature-dependent dynamic viscosity and the Cattaneo-Christov heat-mass flux theory. Therefore, this paper mainly focuses on the analysis of the mixed convection of Casson nanofluid flow as well as heat and mass transfer characteristics in a vertical microchannel filled with a saturated porous medium. The novelty of the present study is to consider temperature-dependent dynamic viscosity, Darcy-Forchheimer porous medium, non-uniform temperature at the permeable walls, and nanofluid injection and suction mechanisms. Moreover, frame-in-different generalizations of the classical Fourier heat conduction law and the Fick molecular mass diffusion law, also known as the Cattaneo-Chirstov heat-mass flux theory, are employed in formulating the governing equations for energy and concentration.

## 2. Mathematical analysis and problem formulation

Let us consider steady mixed convection of Casson nanofluid through a permeable vertical microchannel.

Assume that the permeable walls of the microchannel are positioned at  $(y = 0)$  and  $(y = a)$ , as demonstrated in **Figure 1**, where  $a$  is the width of the microchannel. Also consider the fluid motion is induced by the pressure gradient and the thermal and solutal buoyancy forces. The nanofluid injection  $(y = 0)$  and suction  $(y = a)$  at the walls of the microchannel are also taken into account. Moreover, it is assumed that there is no slip condition at the walls, whereas non-uniform temperatures at the walls are considered in such a way that  $T_0$  is temperature at  $y = 0$  and  $T_w$  is temperature at  $y = a$  with  $T_0 < T_w$ . The dynamic viscosity of the nanofluid is considered to be temperature dependent and written as  $\mu(T) = \mu_0 e^{-\gamma(T-T_0)}$ . Here  $\gamma$  represents viscosity variation coefficient, whereas  $\mu_0$  denotes the left wall dynamic viscosity.

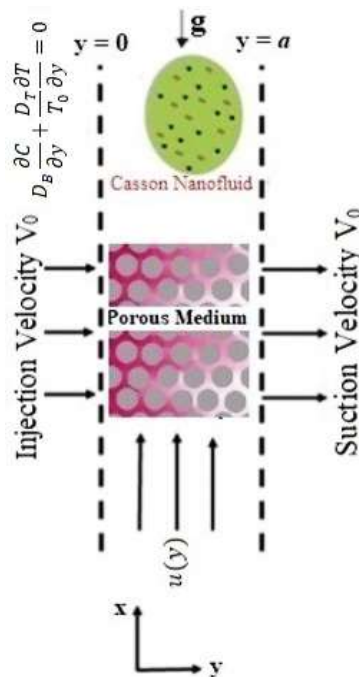


**Figure 1.** Coordinate system and physical flow model.

The non-Newtonian fluid known as Casson was pioneered by Casson<sup>[36]</sup>, in 1959 when he was investigating the flow equations for a pigment oil suspension of printing ink. According to Raza et al.<sup>[27]</sup> the shear stress tensor of the Casson fluid model is given as follows.

$$\tau_{ij} = \begin{cases} \left( \mu_\beta + \frac{P_y}{\sqrt{2\pi}} \right) 2e_{ij}, \pi > \pi_c \\ \left( \mu_\beta + \frac{P_y}{\sqrt{2\pi_c}} \right) 2e_{ij}, \pi < \pi_c \end{cases} \quad (1)$$

Here  $P_y = e_{ij} \cdot e_{ji}$  where  $e_{ij}$  designates rate of deformation at the  $(i, j)^{th}$  component while  $P_y$  represents fluid stress yield. Besides,  $\pi$  denotes product of the component of deformation rate with itself and  $\pi_c$  is a critical value of this product. Similarly,  $\mu_\beta$  denotes plastic dynamic viscosity of the non-Newtonian fluid. Considering the case  $\pi < \pi_c$ , Equation (1) takes the form:

$$\tau_{ij} = \mu_\beta \left( 1 + \frac{1}{\beta} \right) 2e_{ij} \quad (2)$$

where  $\beta = \frac{\mu_\beta \sqrt{2\pi_c}}{P_y}$  represents the Casson fluid parameter and  $e_{ij} = \frac{1}{2} \left( \frac{\partial u_i}{\partial x_j} + \frac{\partial u_j}{\partial x_i} \right)$ .

For two dimensional flows,  $e_{ij} = e_{xy} = \frac{1}{2} \left( \frac{\partial u}{\partial y} + \frac{\partial v}{\partial x} \right) = \frac{1}{2} \left( \frac{\partial u}{\partial y} \right)$ . Therefore, Equation (2) becomes:

$$\tau_{ij} = 2\mu_\beta \left( 1 + \frac{1}{\beta} \right) \frac{1}{2} \left( \frac{\partial u}{\partial y} \right) = \mu_\beta \left( 1 + \frac{1}{\beta} \right) \left( \frac{\partial u}{\partial y} \right) \quad (3)$$

Therefore, by using all the above assumptions and considering the Cattaneo-Christov heat-mass flux theory, under the usual Oberbeck-Boussinesq approximations, the governing PDEs for continuity, energy and concentration equations are given as follows.

$$\frac{\partial u}{\partial x} = 0 \quad (4)$$

$$V_0 \frac{\partial u}{\partial y} = -\frac{1}{\rho} \frac{\partial P}{\partial x} + \frac{1}{\rho} \frac{\partial}{\partial y} \left[ \mu(T) \left( 1 + \frac{1}{\beta} \right) \frac{\partial u}{\partial y} \right] - \frac{\mu(T) \left( 1 + \frac{1}{\beta} \right) u}{\rho K} - \frac{bu^2}{\sqrt{K}} + \beta_1 g(T - T_0) + \beta_2 g(C - C_0) \quad (5)$$

$$V_0 \frac{\partial T}{\partial y} = \alpha_t \frac{\partial^2 T}{\partial y^2} + r \left[ D_B \frac{\partial C}{\partial y} \frac{\partial T}{\partial y} + \frac{D_T}{T_0} \left( \frac{\partial T}{\partial y} \right)^2 \right] + \frac{\mu(T) \left( 1 + \frac{1}{\beta} \right) \left( \frac{\partial u}{\partial y} \right)^2}{(\rho C_p)_{nf}} + \lambda_E V_0^2 \frac{\partial^2 T}{\partial y^2} + \frac{\mu(T) \left( 1 + \frac{1}{\beta} \right) u^2}{(\rho C_p)_{nf} K} + \frac{\rho b u^3}{(\rho C_p)_{nf} \sqrt{K}} \quad (6)$$

$$V_0 \frac{\partial C}{\partial y} = D_B \frac{\partial^2 C}{\partial y^2} + \frac{D_T}{T_0} \frac{\partial^2 T}{\partial y^2} + \lambda_c V_0^2 \frac{\partial^2 C}{\partial y^2} \quad (7)$$

With the boundary conditions:

$$u = 0, v = V_0, T = T_0, D_B \frac{\partial C}{\partial y} + \frac{D_T}{T_0} \frac{\partial T}{\partial y} = 0 \text{ at } y = 0, \quad (8)$$

$$u = 0, v = V_0, T = T_w, C = C_w \text{ at } y = 1$$

where  $u$  is velocity in the axial direction,  $V_0$  is uniform injection/suction velocity,  $a$  is width of the microchannel,  $\rho$  is density of nanofluid,  $P$  is pressure,  $T$  is Temperature of the nanofluid,  $C$  is concentration of nanoparticles,  $C_p$  is specific heat at constant pressure,  $\alpha_t = k/\rho C_p$  is nanofluid thermal diffusivity, with  $k$  signifies thermal conductivity,  $r$  is the ratio of nanoparticles heat capacity and base fluid heat capacity,  $K$  is porous medium permeability,  $g$  is acceleration due to gravity,  $D_B$  is the Brownian diffusion coefficient,  $D_T$  is the thermal diffusion coefficient,  $\beta_1$  is thermal expansion

coefficient,  $\beta_2$  is solutal expansion coefficient,  $\lambda_E$  is thermal relaxation time parameter,  $\lambda_c$  is solutal relaxation time parameter and  $b$  is porous medium inertia resistance coefficient however,  $b = 0$  yields the usual Darcy law.

### 3. Non-dimensionalization

We define the following dimensionless variables for the sake of non-dimensionalization.

$$\begin{aligned} \eta = \frac{y}{a}, \quad \frac{x}{a} = \frac{\rho a u}{\mu_0}, \quad \theta = \frac{T-T_0}{T_1-T_0}, \quad \phi = \frac{C-C_0}{C_1-C_0}, \quad P^* = \frac{a^2 \mu_0 P}{\rho f^2}, \quad A = \frac{\partial P^*}{\partial X}, \\ Re = \frac{\rho a V_0}{\mu_0}, \quad \lambda = \gamma(T_1 - T_0), \quad \lambda_e = \lambda_E \frac{V_0^2 \rho}{\mu_0}, \quad \lambda_c = \lambda_c \frac{V_0^2 \rho}{\mu_0}, \quad S = \frac{K}{a^2}, \\ F = \frac{ba}{\rho \sqrt{K}}, \quad Gt = \frac{\beta_1 g \rho^2 a^3 (T_1 - T_0)}{\mu_0^2}, \quad Gc = \frac{\beta_2 g \rho^2 a^3 (C_1 - C_0)}{\mu_0^2}, \quad Nt = \Gamma \frac{D_T (T_1 - T_0)}{T_0} \frac{\rho}{\mu_0}, \\ Nb = \Gamma D_{B(C_1 - C_0)} \frac{\rho}{\mu_0}, \quad Ec = \frac{\mu_0^2}{\rho^2 a^2 C_p (T_1 - T_0)}, \quad Pr = \frac{\mu_0}{\rho \alpha}, \quad Sc = \frac{\mu_0}{\rho D_B} \end{aligned} \tag{9}$$

Using the dimensionless variables in Equation (9), Equations (4)–(8) take the following forms.

$$\frac{\partial W}{\partial X} = 0 \tag{10}$$

$$Re \frac{\partial W}{\partial \eta} = A + e^{-\lambda \theta} \left( 1 + \frac{1}{\beta} \right) \left[ \frac{\partial^2 W}{\partial \eta^2} - \lambda \frac{\partial \theta}{\partial \eta} \frac{\partial W}{\partial \eta} \right] - e^{-\lambda \theta} \left( 1 + \frac{1}{\beta} \right) S^2 W - FW^2 + Gt\theta + Gc\phi \tag{11}$$

$$Re \frac{\partial \theta}{\partial \eta} = \left( \lambda_e + \frac{1}{Pr} \right) \frac{\partial^2 \theta}{\partial \eta^2} + Nb \frac{\partial \phi}{\partial \eta} \frac{\partial \theta}{\partial \eta} + Nt \left( \frac{\partial \theta}{\partial \eta} \right)^2 + Ece^{-\lambda \theta} \left( 1 + \frac{1}{\beta} \right) \left( \frac{\partial W}{\partial \eta} \right)^2 + S^2 Ece^{-\lambda \theta} \left( 1 + \frac{1}{\beta} \right) W^2 + FEcW^3 \tag{12}$$

$$Re \frac{\partial \phi}{\partial \eta} = \frac{1}{Sc} \left[ (1 + \lambda_c) \frac{\partial^2 \phi}{\partial \eta^2} + \frac{Nt}{Nb} \frac{\partial^2 \theta}{\partial \eta^2} \right] \tag{13}$$

With the dimensionless boundary conditions:

$$\begin{aligned} W = 0, \quad \theta = 0, \quad Nb \frac{\partial \phi}{\partial \eta} + Nt \frac{\partial \theta}{\partial \eta} = 0 \text{ at } \eta = 0, \\ W = 0, \quad \theta = 1, \quad \phi = 1 \text{ at } \eta = 1 \end{aligned} \tag{14}$$

where,  $Re$  is the suction/injection Reynolds number,  $Gt$  is thermal Grashof number,  $Gc$  is solutal Grashof number,  $Ec$  is the Eckert number,  $Pr$  is the Prandtl number,  $A$  is dimensionless pressure gradient parameter,  $\lambda$  is dimensionless viscosity variation parameter,  $\lambda_e$  is dimensionless thermal relaxation time parameter,  $\lambda_c$  is dimensionless solutal relaxation time parameter,  $S$  is porous medium shape factor parameter,  $F$  is the Forchheimer number,  $Sc$  is the Schmidt number,  $Nb$  is the Brownian motion parameter and  $Nt$  is the thermophoresis parameter.

Actually, the continuity Equation (10),  $\frac{\partial W}{\partial X} = 0$  suggests that  $W$  is as a function of  $\eta$  only. Therefore, the dimensionless governing Equations (11)–(14) are ODEs with respect to  $\eta$  only and written as follows.

$$ReW' = A + e^{-\lambda \theta} \left( 1 + \frac{1}{\beta} \right) (W'' - \lambda \theta' W') - e^{-\lambda \theta} \left( 1 + \frac{1}{\beta} \right) S^2 W - FW^2 + Gt\theta + Gc\phi \tag{15}$$

$$\begin{aligned} Re\theta' = \left( \lambda_e + \frac{1}{Pr} \right) \theta'' + Nb\phi'\theta' + Nt\theta'' + Ece^{-\lambda \theta} \left( 1 + \frac{1}{\beta} \right) W'' \\ + S^2 Ece^{-\lambda \theta} \left( 1 + \frac{1}{\beta} \right) W^2 + FEcW^3 \end{aligned} \tag{16}$$

$$Re\phi' = \frac{1}{Sc} \left[ (1 + \lambda_c)\phi'' + \frac{Nt}{Nb}\theta'' \right] \quad (17)$$

With the dimensionless boundary conditions:

$$\begin{aligned} W = 0, \theta = 0, Nb\phi' + Nt\theta' = 0 \text{ at } \eta = 0, \\ W = 0, \theta = 1, \phi = 1 \text{ at } \eta = 0 \end{aligned} \quad (18)$$

There are also physical quantities of engineering interests including coefficient of the skin friction  $C_f$ , the Nusselt number  $Nu$  (wall heat transfer rate) and the Sherwood number  $Sh$  (wall mass transfer rate). Therefore, the non-dimensional forms are given below.

$$C_f = e^{-\lambda\theta} \left( 1 + \frac{1}{\beta} \right) \frac{dW}{d\eta} \Big|_{\eta=0,1}, \quad Nu = - \frac{d\theta}{d\eta} \Big|_{\eta=0,1}, \quad Sh = - \frac{d\phi}{d\eta} \Big|_{\eta=0,1} \quad (19)$$

## 4. Numerical solutions

In this study, the numerical simulation is done via the Keller-Box method. The Keller-Box is a second-order accurate implicit finite difference scheme that was named after the pioneering work of Cebeci and Bradshaw<sup>[37]</sup>. Indeed, the Keller-Box is stable unconditionally and comprises attractive extrapolation features with arbitrary spacing. The scheme consists of the following four crucial steps:

- Reducing the second order ODEs into a system of first order equations.
- Finite difference discretization of a system of first order equations.
- Linearizing the resulting algebraic equations by using the Newton method and writing in matrix-vector form.
- Solving the linearized system of equations using the block-tridiagonal elimination technique.

Therefore, the Keller-Box method is employed to solve the non-linear ODEs (15)– (17) along the boundary conditions (18).

## 5. Results and discussions

### 5.1. The velocity, temperature and concentration profiles

The influence of the Casson fluid parameter on the velocity and temperature of the nanofluid are portrayed in **Figures 2a** and **2b**, respectively. Accordingly, within the microchannel core region both velocity and temperature of the nanofluid increase with  $\beta$ . This is the case because as  $\beta$  increases, the yield stress dominates the dynamic viscosity of the nanofluid. Remarkably, as  $\beta \rightarrow \infty$  the Casson fluid have a tendency of performing like Newtonian fluid. This result is similar to the findings of Reddy et al.<sup>[5]</sup> and Roja et al.<sup>[38]</sup>. As values of the variable viscosity parameter  $\lambda$  rise, both velocity and temperature of the nanofluid increase significantly as displayed in **Figures 3a** and **3b** respectively. Indeed, this result is expected because  $\mu(\theta) = \mu_0 e^{-\lambda\theta}$  which implies that the dynamic viscosity decreases as  $\lambda$  increases and hence it is favourable for fluid motion that also in turn leads to an increase in the nanofluid temperature. Similar result was reported by Mahmoudi et al.<sup>[39]</sup>.

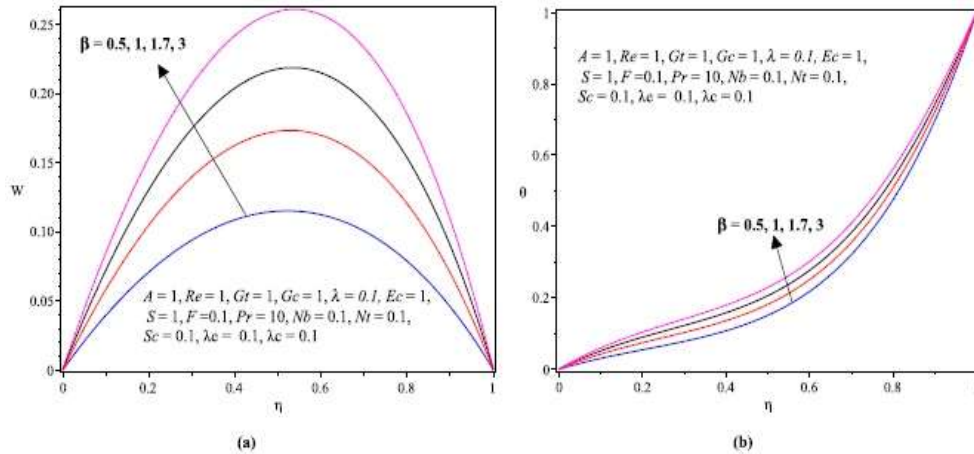


Figure 2. (a) velocity and; (b) temperature profiles with increasing  $\beta$ .

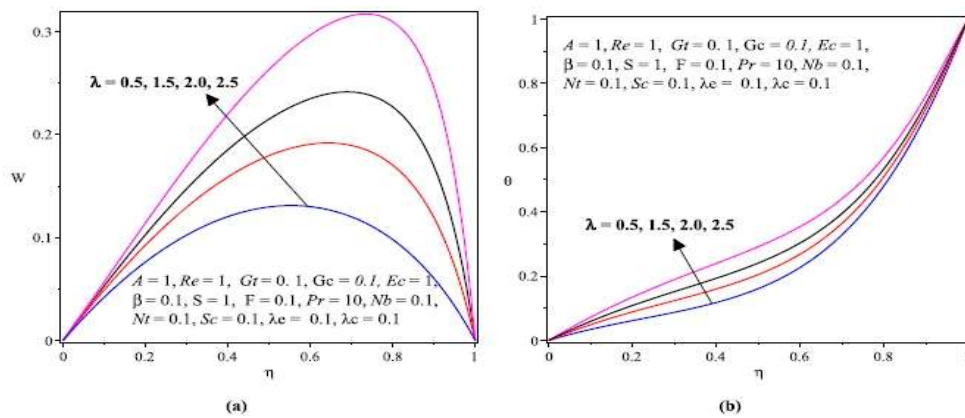


Figure 3. (a) velocity and; (b) temperature profiles with increasing  $\lambda$ .

Figure 4a depicts that the nanofluid concentration profile decreases as the values of the Casson fluid parameter  $\beta$  increases. Actually, this is the opposite scenario to the effect of  $\beta$  on the temperature profile (see Figure 3b). The secret behind this result is the fact called the effect of the cross-diffusion meaning a small increase in temperature of the nanofluid may result in a small decrease in the concentration of the nanoparticles and vice versa. By the same argument, the nanoparticle concentration profile decreases when the magnitude of  $\lambda$  increases as demonstrated in Figure 4b.

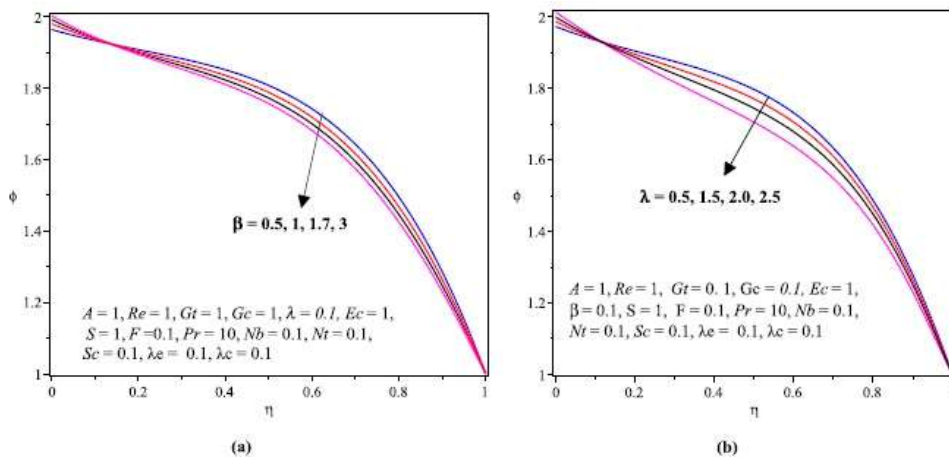


Figure 4. (a) effects of (a)  $\beta$  and (b)  $\lambda$  on concentration profile.

The impacts of the thermal buoyancy parameter  $Gt$  (thermal Grashof number) and the solutal buoyancy parameter  $Gc$  (solutal Grashof number), respectively, on the nanofluid velocity and temperature are presented in **Figures 5a** and **5b** and **Figures 6a** and **6b**. Consequently, these figures show that the nanofluid velocity and temperature escalate with rising magnitudes of  $Gt$  and  $Gc$ . Physically, as  $Gt$  and  $Gc$  increase, the buoyancy forces due to the differences in temperature and concentration respectively also increase that obviously increases the nanofluid velocity, which in turn increases the viscous heating within fluid layers. So, the temperature profile also enhances inside the microchannel core region. However, **Figures 7a** and **7b** demonstrate the reverse situations in the case of the concentration of the nanoparticles.

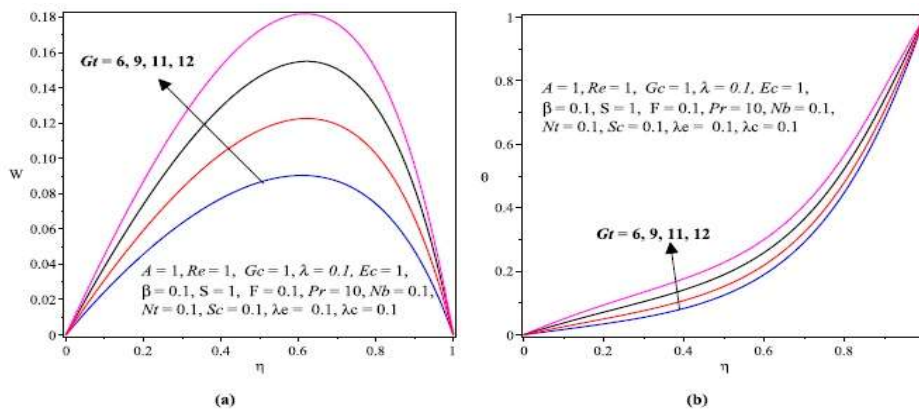


Figure 1. (a) velocity and (b) temperature profiles with increasing  $Gt$ .

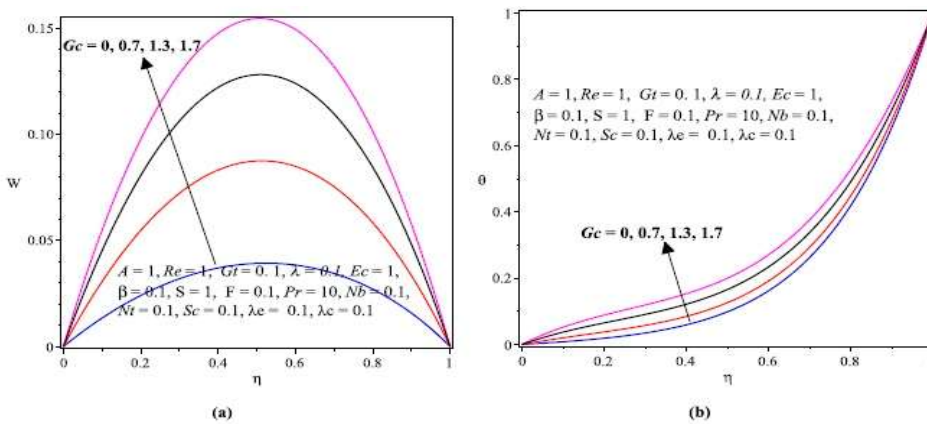


Figure 2. (a) velocity and (b) temperature profiles with increasing  $Gc$ .

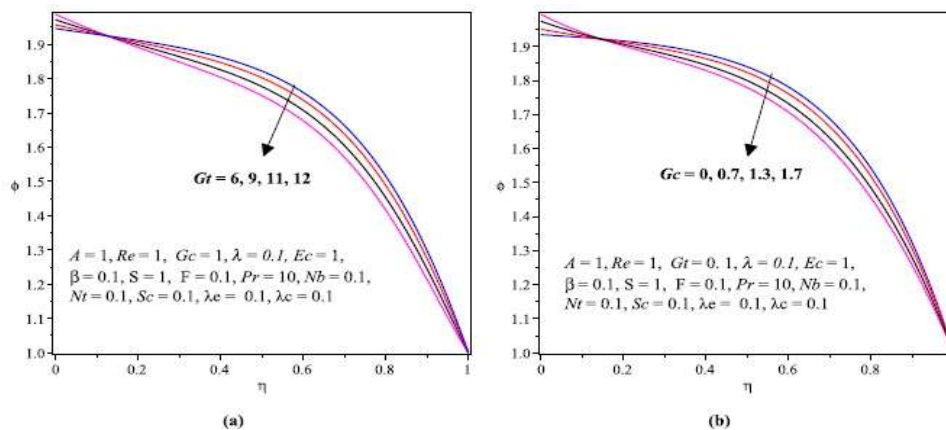
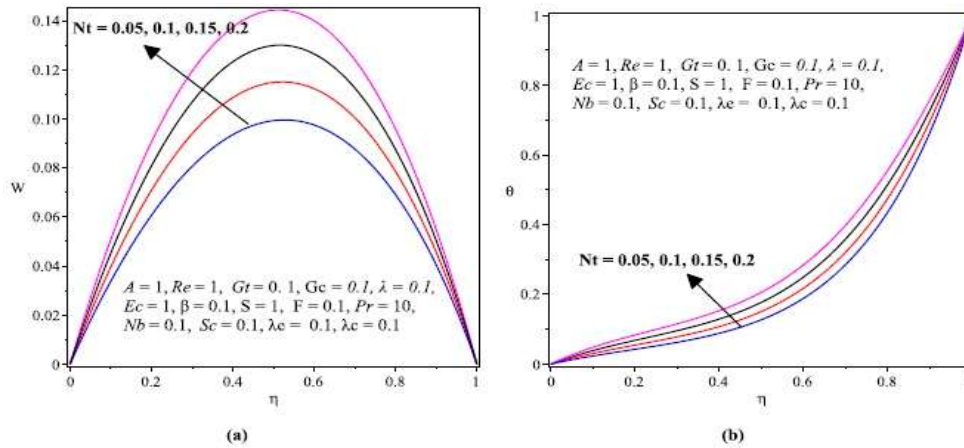


Figure 3. (a) effects of (a)  $Gt$  and (b)  $Gc$  on concentration profile.

The influences of thermophoresis parameter  $Nt$  on the nanofluid velocity and temperature are portrayed in **Figures 8a** and **8b** respectively. Hence, the nanofluid velocity and temperature escalate as the amounts of  $Nt$  increase. Physically, the thermophoretic force gets stronger when the amounts of  $Nt$  rises that will lead to the migration of nanoparticles from the hot microchannel walls to the cold fluid throughout the core flow region. Therefore, the temperature profile enhances which in turn enhances the velocity profile with increasing amounts of  $Nt$ .



**Figure 4.** (a) velocity and (b) temperature profiles with increasing  $Nt$ .

**Figures 9a** and **9b** are graphs that show the nanofluid velocity and temperature fall as the magnitudes of the parameters of Brownian motion  $Nb$  upsurge. Physically, when the values of  $Nb$  escalate, the random and non-uniform movements of the nanoparticles inside the microchannel core region also enhance, which will lead to the increment of collisions between the moving base fluid molecules and the nanoparticles. Therefore, these increments in collisions may cause the retardation of fluid motion and hence its velocity. Moreover, when nanofluid moves slowly, its temperature also reduces due to the lessened fluid kinetic energy.

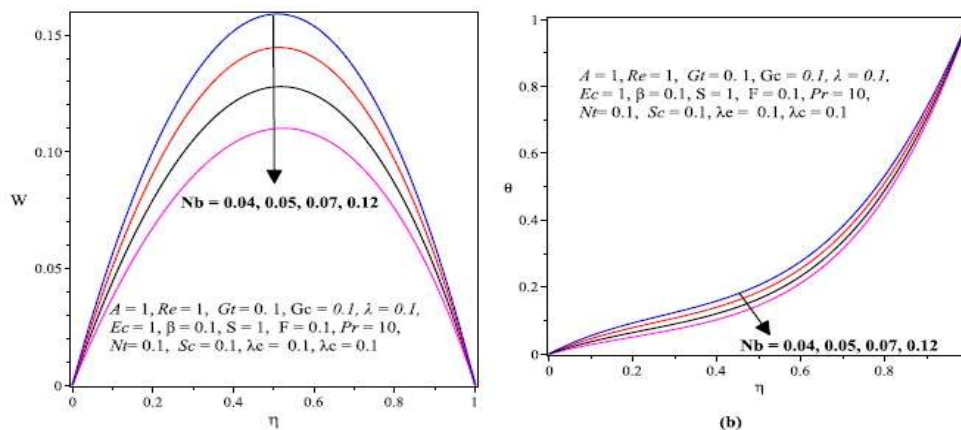


**Figure 5.** (a) velocity and (b) temperature profiles with increasing  $Nb$ .

**Figure 10a** indicates that as the amounts of  $Nt$  upsurges, the nanoparticle concentration also enhances. An argument for this result may be the fact that when the amounts of  $Nt$  rises, the thermophoretic force gets stronger that will lead to the migration of nanoparticles from hot microchannel walls to the cold fluid, and thus the concentration of the nanoparticles enhances throughout the core flow region. But **Figure 10b** reveals that the nanoparticle concentration diminishes

as the magnitudes of the parameters of Brownian motion  $Nb$  rise. Physically, when the values of  $Nb$  escalate, the random and non-uniform movements of the nanoparticles inside the microchannel core flow region also enhance that will lead to the increment of collisions between the moving base fluid molecules and the nanoparticles. Therefore, these increments of collisions and random movement of nanoparticles may cause the diminishing of nanoparticles concentration throughout the core flow region.

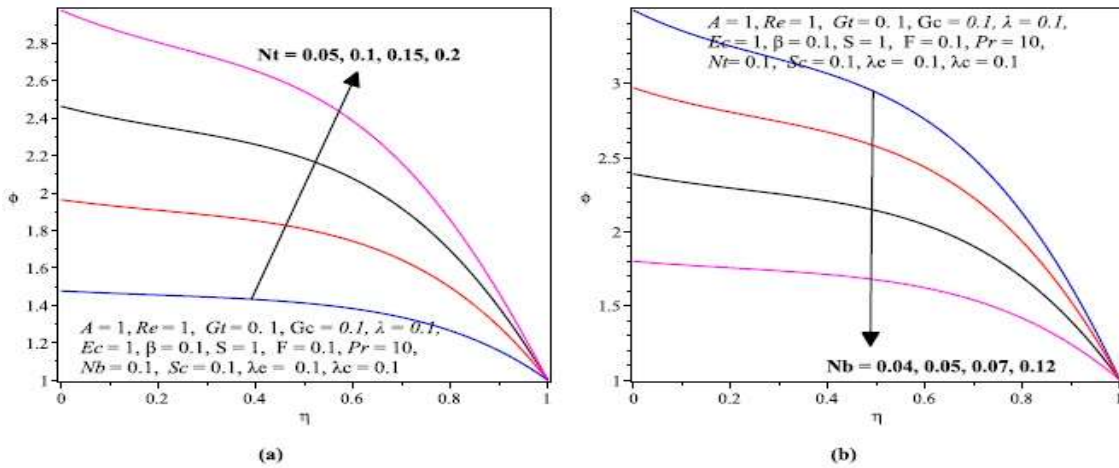


Figure 6. (a) effects of (a)  $Nt$  and (b)  $Nb$  on concentration profile.

Figures 11a and 11b display that the Schmidt number  $Sc$  indicates a rising effect on the nanofluid velocity and temperature, respectively. Similarly, the concentration profile increases with increasing values of  $Sc$  (see Figure 12a). Indeed, the justification is the fact that as the amount of  $Sc$  enhances the amount of molecular mass diffusion within the fluid reduces, as a result of which the nanoparticle concentration stays higher throughout the microchannel core flow region. Figure 12b portrays the effect of the solutal relaxation time parameter  $\lambda_c$  on the concentration profile. As it can be seen from the graph, when magnitude of  $\lambda_c$  increases the nanoparticle concentration decreases.

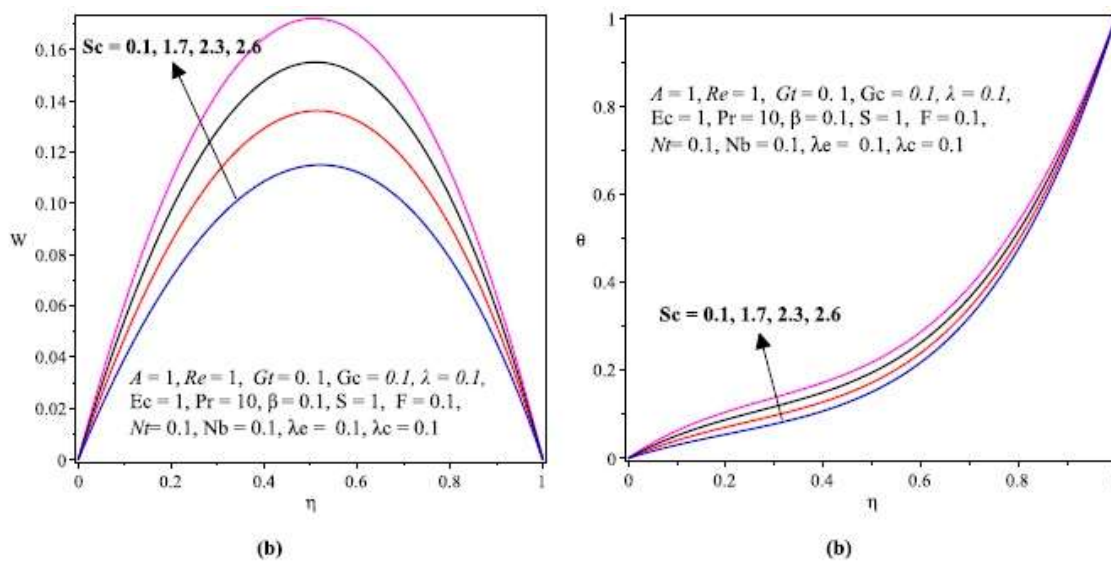


Figure 7. (a) velocity and (b) temperature profiles with increasing  $Sc$ .

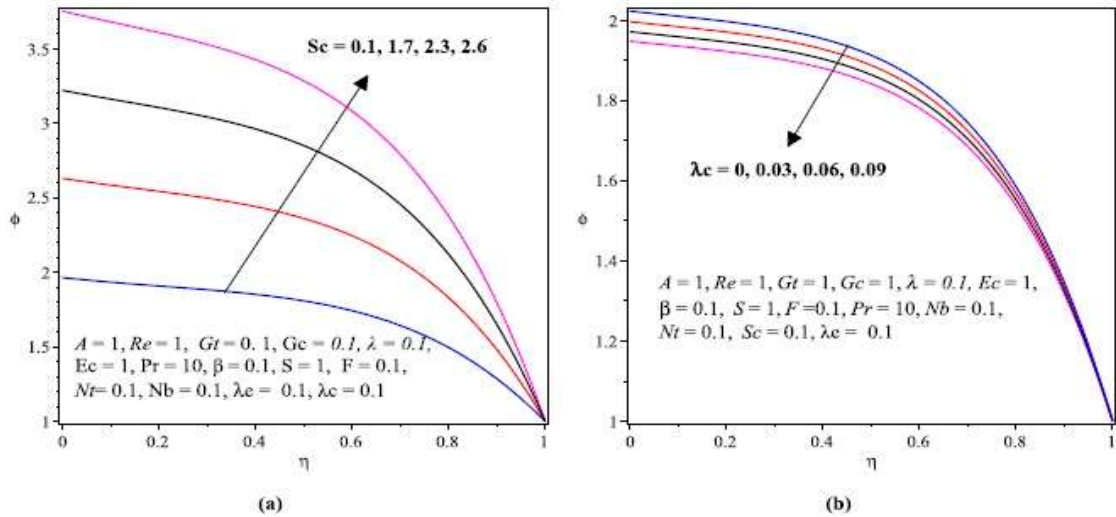


Figure 8. (a) effects of (a)  $Sc$  and (b)  $\lambda_c$  on concentration profile.

Figure 13a depicts that the nanofluid velocity reduces considerably with an increasing amount of  $S$  (porous medium shape factor parameter). Mahmoudi et al.<sup>[39]</sup> and Kasaejan et al.<sup>[42]</sup> presented similar findings. This is the case because the permeability of the porous medium and  $S$  are inversely related so that the nanofluid velocity decreases with increasing amount of  $S$ . Likewise, the nanofluid velocity declines noticeably with increasing amount of  $F$  (the Forchheimer number), since  $F$  represents the inertial resistivity force, which obviously opposes the nanofluid motion and therefore, declines the velocity profile.

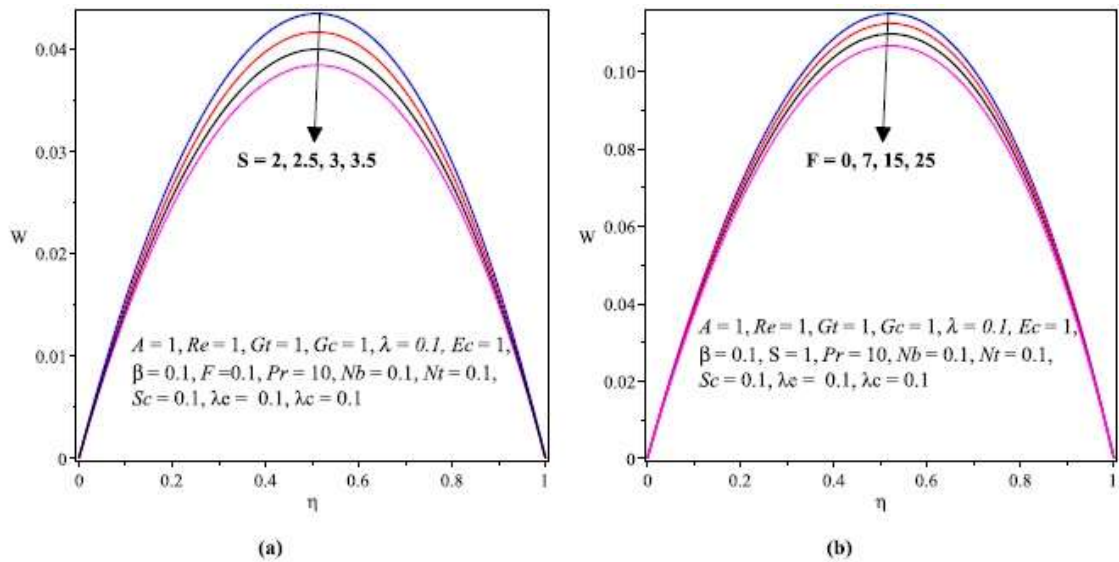


Figure 9. (a) effects of (a)  $S$  and (b)  $F$  on velocity profile.

Figures 14a and 14b are graphs that show the impacts of the Eckert number  $Ec$  on temperature and nanoparticle concentration respectively. The temperature profile enhances with increasing values  $Ec$  as provided in Figure 9a. This is the case since  $Ec$  describes viscous heating between the fluid layers and thus the nanofluid temperature enhances as the value of  $Ec$  rises. From the references<sup>[39-41]</sup>, a comparable outcome was reported. Figure 14b displays a reverse situation in the case of the nanoparticle concentration.

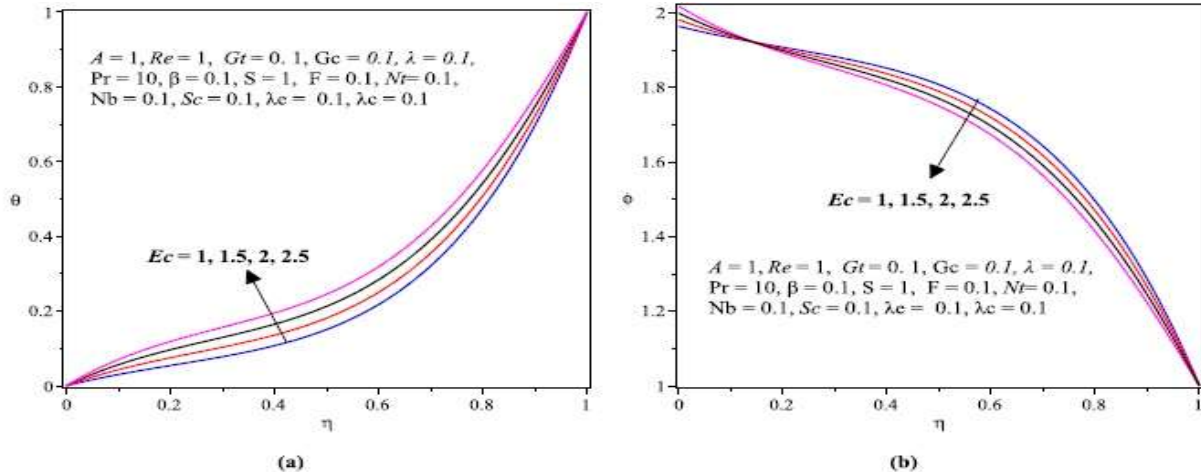


Figure 10. (a) temperature and; (b) concentration profiles with increasing  $Ec$ .

The influences of the Prandtl number  $Pr$  on the nanofluid temperature and the nanoparticle concentration are displayed in **Figures 15a** and **15b** respectively. Therefore, the nanofluid temperature decreases with escalating amounts of  $Pr$  because a high amount of  $Pr$  implies less amount of fluid thermal diffusivity within the microchannel core flow region, as a result of which the nanofluid temperature remains lower throughout the core flow region (see **Figures 15a**). An analogous result was given in Kasaejan et al.<sup>[42]</sup> and Menni et al.<sup>[43]</sup> while Mahmoudi et al.<sup>[39]</sup> reported a conflicting result. Contrastingly, **Figure 15b** presents that the nanoparticle concentration escalates when the size of  $Pr$  upsurges.

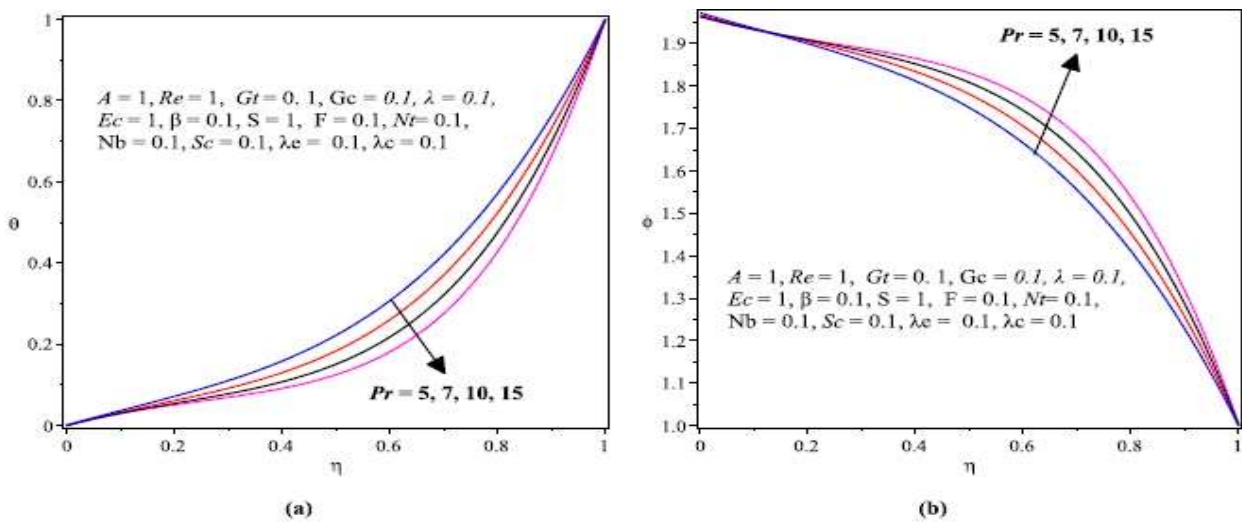


Figure 11. (a) temperature and; (b) concentration profiles with increasing  $Pr$ .

The influences of the thermal relaxation time parameter  $\lambda_e$  on the nanofluid temperature and the nanoparticle concentration are indicated in **Figures 16a** and **16b** respectively. Accordingly, **Figure 16a** indicates that a larger value of  $\lambda_e$  yields a larger amount of nanofluid temperature. In fact, thermal relaxation time is amount of time that the fluid requires to transfer heat into its surroundings and therefore, bigger value of  $\lambda_e$  indicates the fluid needs more extra time to transfer heat so that its temperature remains higher. Here, for  $\lambda_e = 0$ , heat transfers slowly throughout the microchannel walls and hence fluid temperature distribution is lower for the classical Fourier heat conduction law. That is, the Cattaneo-Christov heat flux model is beneficial for microfluidics systems with high heat. An

equivalent finding was reported by Mahanthesh et al.<sup>[33]</sup> and Nayak et al.<sup>[44]</sup>. The opposite scenario was observed for the nanoparticle concentration with  $\lambda e$  (see **Figure 16b**).

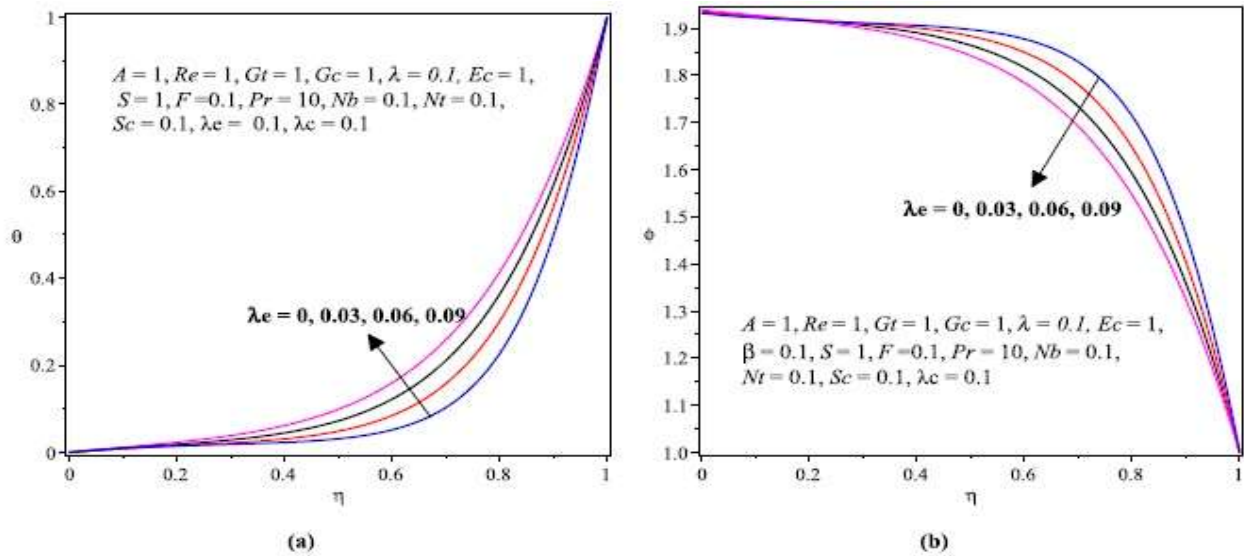


Figure 12. (a) temperature and; (b) concentration profiles with increasing  $\lambda e$ .

### 5.2. Skin friction coefficient (wall shear stress)

Figures 17a–19b illustrate the impacts of the embedded governing thermophysical parameters on the skin friction coefficient at the left wall ( $\eta = 0$ ) as well as right wall ( $\eta = 1$ ) of the microchannel. As a consequence, the figures present that the skin friction coefficient  $C_f$  at  $\eta = 0$  and  $\eta = 1$  increase as the magnitudes of the pressure gradient parameter  $A$ , Eckert number  $Ec$ , Forchheimer number  $F$  and injection/suction Reynolds number  $Re$  increase. Mahmoudi et al.<sup>[39]</sup> found a similar research result. Thermal Grashof number  $Gt$  shows a decreasing effect on  $C_f$  at  $\eta = 0$  and  $\eta = 1$ . Moreover,  $C_f$  rises at  $\eta = 0$  (see **Figure 19a**) but  $C_f$  falls down at  $\eta = 1$  (refer **Figure 19b**) with increasing values of  $\lambda$ . However, the Casson fluid parameter  $\beta$  shows the opposite effects on  $C_f$  at  $\eta = 0$  and  $\eta = 1$  as presented in **Figures 17a** and **17b** respectively.

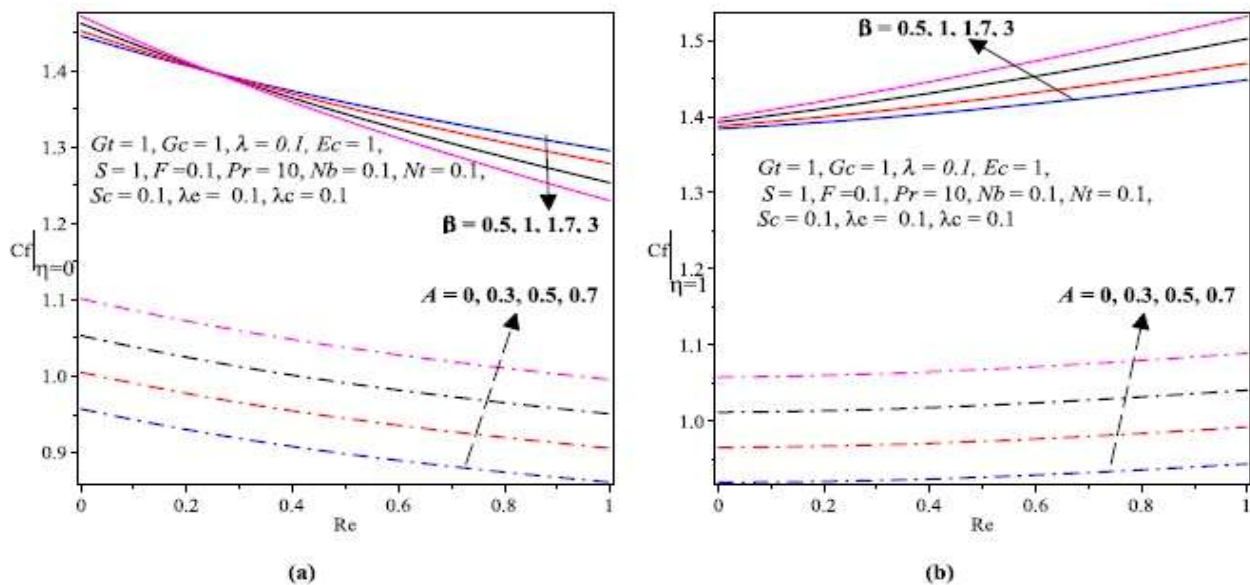


Figure 13. (a)  $C_f$  at  $\eta = 0$  and; (b)  $C_f$  at  $\eta = 1$  with increasing  $\beta, A, Re$ .

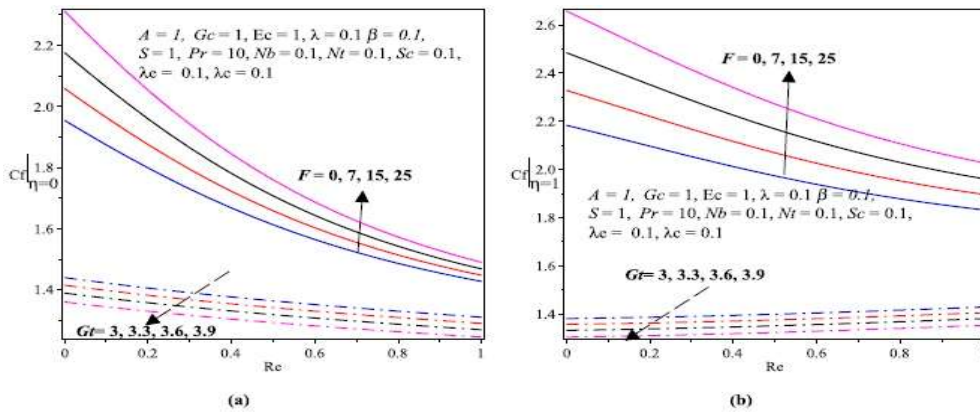


Figure 14. (a)  $C_f$  at  $\eta = 0$  and; (b)  $C_f$  at  $\eta = 1$  with increasing  $Gt, F, Re$ .

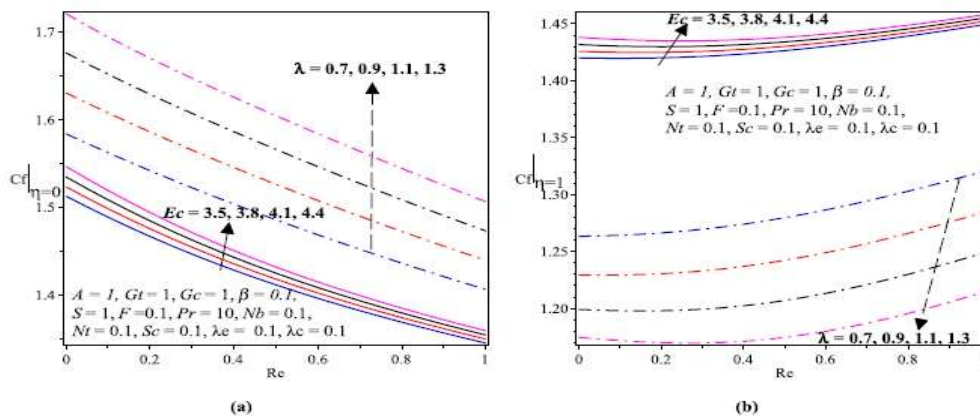


Figure 15. (a)  $C_f$  at  $\eta = 0$  and; (b)  $C_f$  at  $\eta = 1$  with increasing  $Ec, \lambda, Re$ .

### 5.3. The nusselt number (wall heat transfer rate)

Figures 20a–23b illustrate the impacts of the embedded governing thermophysical parameters on the Nusselt number  $Nu$  at the left wall ( $\eta = 0$ ) as well as right wall ( $\eta = 1$ ) of the microchannel. As a consequence, the figures reveal that  $Nu$  at  $\eta = 0$  and  $\eta = 1$  increase as the values of  $\lambda, Ec$  and  $Re$  increase. Mahmoudi et al.<sup>[39]</sup> found a similar research result. Moreover, as the magnitude of  $\beta, A, Pr$ , and  $Nt$  increase,  $Nu$  at  $\eta = 0$  shows a rising tendency but it shows a decreasing trend at  $\eta = 1$ . Besides,  $Nb$  and  $\lambda_e$  indicate the opposite scenarios on  $Nu$  at  $\eta = 0$  and at  $\eta = 1$ .

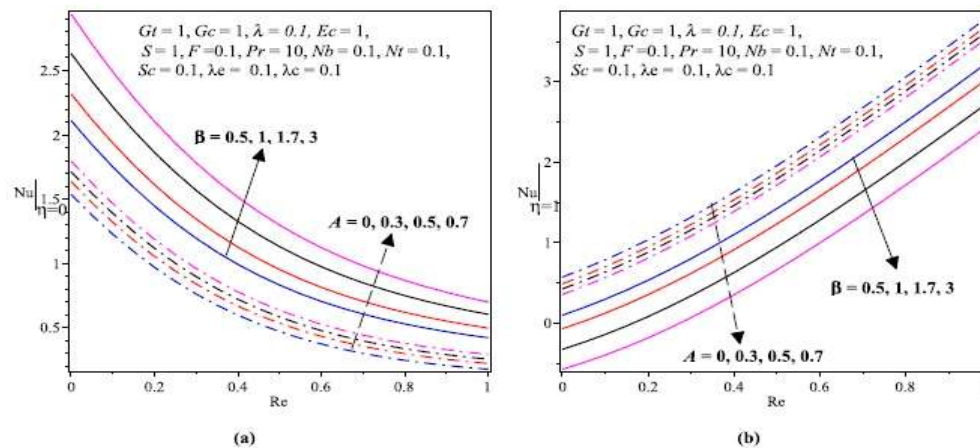


Figure 16. (a)  $Nu$  at  $\eta = 0$  and; (b)  $Nu$  at  $\eta = 1$  with increasing  $\beta, A, Re$ .

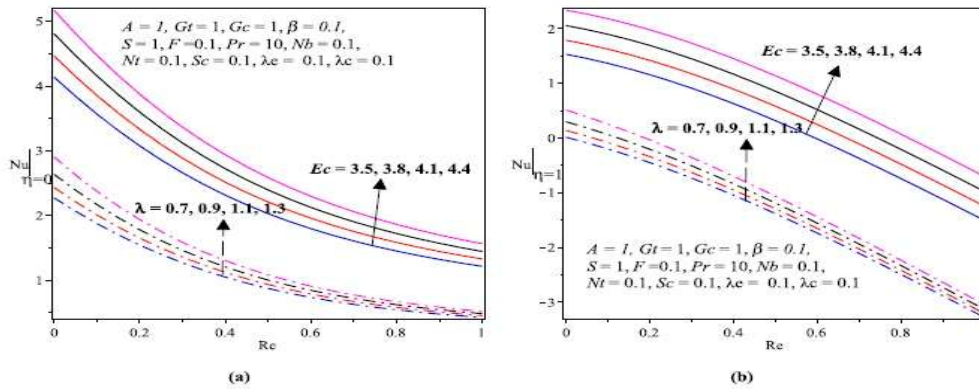


Figure 17. (a)  $Nu$  at  $\eta = 0$  and; (b)  $Nu$  at  $\eta = 1$  with increasing  $Ec, \lambda, Re$ .

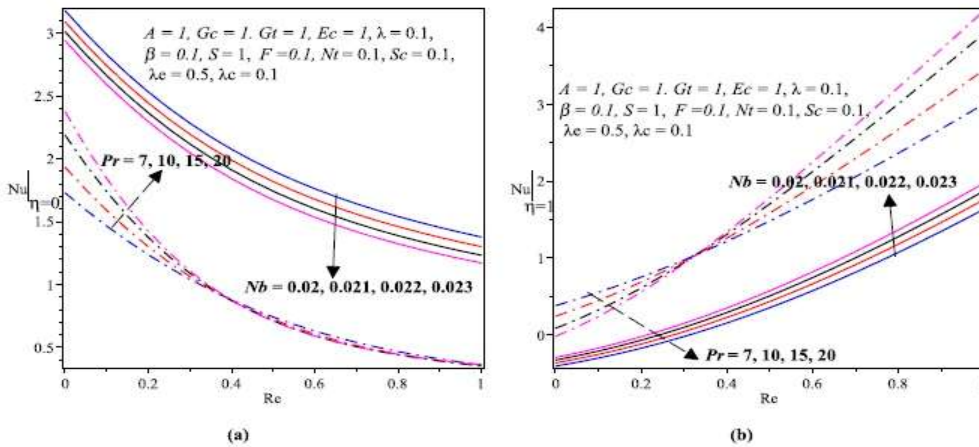


Figure 18. (a)  $Nu$  at  $\eta = 0$  and; (b)  $Nu$  at  $\eta = 1$  with increasing  $Pr, Nb, Re$ .

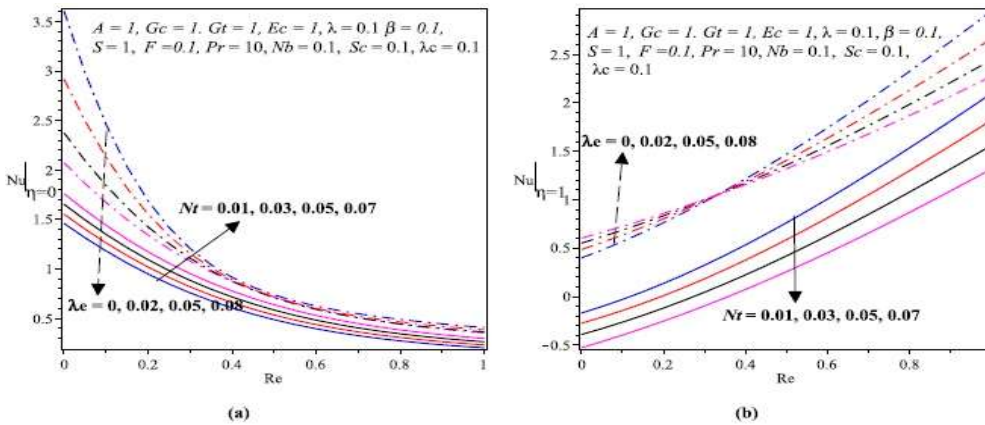


Figure 19. (a)  $Nu$  at  $\eta = 0$  and; (b)  $Nu$  at  $\eta = 1$  with increasing  $Nt, \lambda_e, Re$ .

#### 5.4. The sherwood number (wall mass transfer rate)

Figures 24a–27b portray the influences of the embedded governing thermophysical parameters on the Sherwood number  $Sh$  at the left wall ( $\eta = 0$ ) as well as right wall ( $\eta = 1$ ) of the microchannel. As a result, these graphs depict that  $Sh$  at  $\eta = 0$  and  $\eta = 1$  increase as the values of  $\lambda, Ec, Sc$  and  $Re$  increase. Nonetheless,  $\lambda_e$  and  $\lambda_c$  show a diminishing consequence on  $Sh$  at  $\eta = 0$  and  $\eta = 1$ . Moreover, as the magnitude of  $\beta, A, Pr,$  and  $Nt$  increase,  $Nu$  at  $\eta = 0$  shows a rising tendency, but it shows a decreasing trend at  $\eta = 1$ . Besides,  $Nb$  and  $\lambda_e$  indicate the opposite scenarios on  $Nu$  at  $\eta = 0$  and at  $\eta = 1$ .

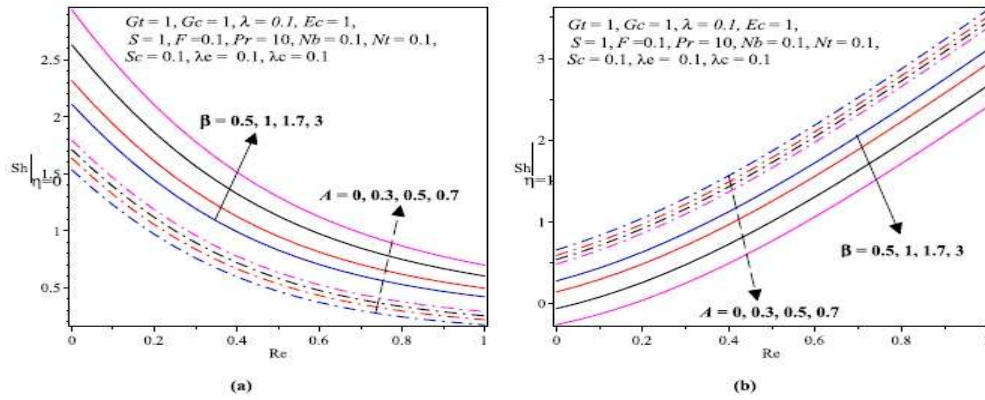


Figure 20. (a)  $Sh$  at  $\eta = 0$  and; (b)  $Sh$  at  $\eta = 1$  with increasing  $\beta, A, Re$ .

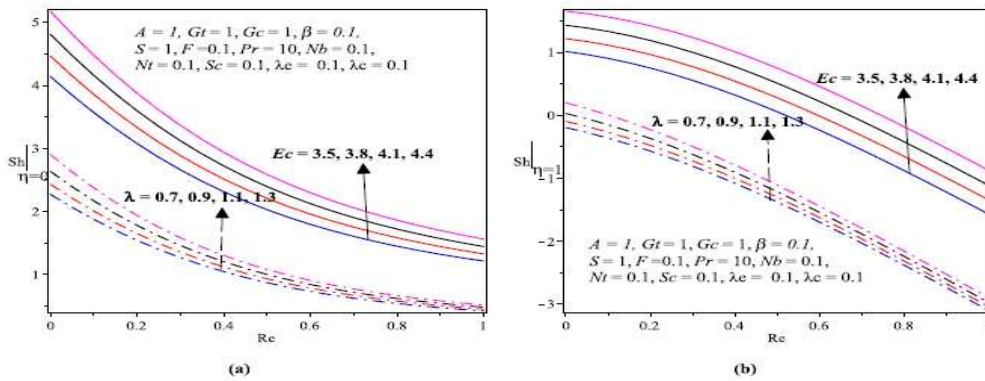


Figure 21. (a)  $Sh$  at  $\eta = 0$  and; (b)  $Sh$  at  $\eta = 1$  with increasing  $Ec, \lambda, Re$ .

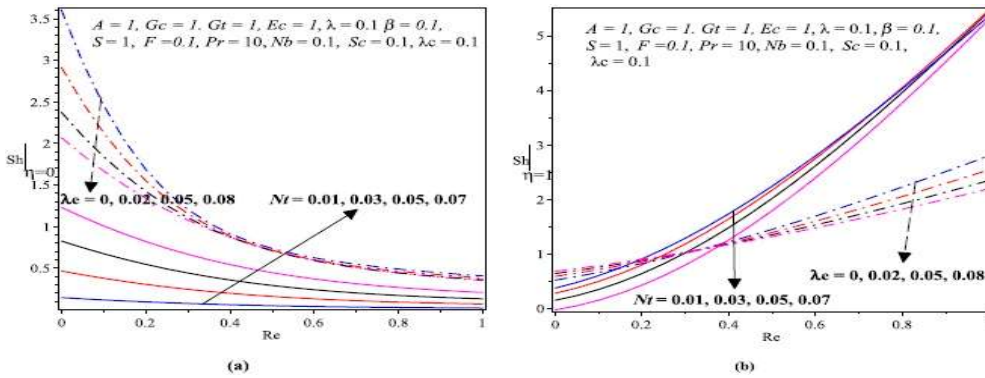


Figure 22. (a)  $Sh$  at  $\eta = 0$  and; (b)  $Sh$  at  $\eta = 1$  with increasing  $Nt, \lambda_e, Re$ .

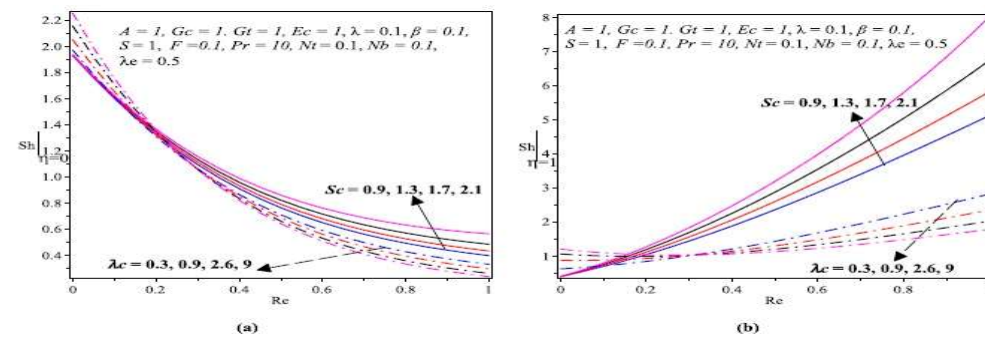


Figure 23. (a)  $Sh$  at  $\eta = 0$  and; (b)  $Sh$  at  $\eta = 1$  with increasing  $Sc, \lambda_c, Re$ .

## 6. Conclusions

Thermal behaviours and hydrodynamics of non-Newtonian nanofluids flow through permeable microchannels have large-scale utilization in industries, engineering, and biomedicine. Hence, this paper mainly focuses on the analysis of mixed convection of Casson nanofluid flow as well as heat and mass transfer characteristics in a vertical microchannel filled with a saturated porous medium. The highly nonlinear PDEs corresponding to the continuity, momentum, energy, and concentration equations are formulated and solved numerically via the second-order implicit finite difference scheme known as the Keller-Box method. Therefore, depending on the results obtained from the present analysis, the key conclusions are given as follows.

- Both nanofluid velocity and temperature indicate a rising trend as the values of  $\beta$ ,  $\lambda$ ,  $Gt$ ,  $Gc$ ,  $Sc$ ,  $Nt$  and  $Sc$  increase.
- The porous medium dampens the nanofluid motion as well as the nanofluid temperature distributions.
- The temperature profile escalates with increasing values of  $Ec$  and  $\lambda e$  however it falls with  $Pr$ .
- The effect of the Brownian motion is opposite on the nanofluid velocity and temperature profiles.
- The nanoparticle concentration increases with  $Pr$ ,  $Sc$  and  $Nt$ .
- The skin friction coefficient  $C_f$  shows an increasing behavior as the values of  $A$ ,  $Ec$ ,  $F$  and  $Re$  increase.
- The Nusselt number  $Nu$  demonstrates an enhancing pattern when the magnitudes of  $Ec$ ,  $\lambda$  and  $Re$  rise.
- $\beta$  and  $\lambda e$  reveal opposite scenarios on the Nusselt number  $Nu$  at the left and right walls of the microchannel.
- The mass transfer rate  $Sh$  at both walls of the microchannel shows an increasing pattern with increasing values of  $Ec$ ,  $\lambda$ ,  $Sc$  and  $Re$ .

## Author contributions

Conceptualization, EHR and LGE; methodology, EHR; software, EHR; validation, EHR, LGE and AFG; formal analysis, EHR; investigation, EHR; resources, EHR; data curation, EHR; writing—original draft preparation, EHR; writing—review and editing, AFG; visualization, EHR; supervision, LGE; project administration, AFG; funding acquisition, LGE. All authors have read and agreed to the published version of the manuscript.

## Acknowledgments

The authors are grateful to the financial support of Adama Science and Technology University.

## Conflict of interest

The authors declare no conflict of interests.

## Nomenclature

$a$	Microchannel width	$k$	thermal conductivity
$A$	Dimensionless nanofluid pressure	$Nb$	Brownian motion parameter
$b$	Porous inertial resistance coefficient	$Nt$	Thermophoresis parameter

$C$	Chemical species concentration	$P$	Pressure of nanofluid
$C_f$	Coefficient of skin friction	$Pr$	Prandtl number
$C_p$	Specific heat at constant pressure	$Nu$	Nusselt number
$D_b$	Brownian diffusion coefficient	$Re$	Injection/suction Reynolds number
$D_T$	Thermal diffusion coefficient	$S$	Porous medium shape factor parameter
$Ec$	Eckert number	$Sc$	Schmidt number
$F$	Forchheimer number	$Sh$	Sherwood number
$g$	Gravitational acceleration	$T$	Temperature of nanofluid
$Gc$	Solutal Grashof number	$(u, v)$	Velocity components
$Gr$	Thermal Grashof number	$V_0$	Wall suction/injection velocity
$K$	Permeability parameter	$W$	Dimensionless axial velocity
$(x, y)$	Cartesian coordinates	$X$	Dimensionless axial axis

#### Greek Symbols

$\beta$	Casson fluid parameter	$\gamma_1$	Viscosity variation parameter
$\beta_1$	Coefficient of thermal expansion	$\eta$	Dimensionless normal axis
$\beta_2$	Coefficient of solutal expansion	$\theta$	Dimensionless temperature
$\gamma$	Heat capacity ratio	$\mu(T)$	Temperature dependent dynamic viscosity
$\lambda$	Dimensionless variable viscosity	$\tau_w$	Wall shear stress
$\lambda_e$	Dimensionless thermal relaxation	$\rho$	Nanofluid density
$\lambda_c$	Dimensionless concentration relaxation	$\phi$	Dimensionless nanoparticles concentration

## References

- Bergman TL, Lavine AS, Incropera FP, DeWitt DP. *Fundamentals of Heat and Mass Transfer*. Wiley & Sons; 2011.
- Holman JP. *Heat Transfer*, 10th ed. McGraw-Hill Education; 2010.
- Tuckerman DB, Pease RFW. High-performance heat sinking for VLSI. *IEEE Electron Device Letters* 1981; 2(5): 126–129. doi: 10.1109/EDL.1981.25367
- Saleel CA, Algahtani A, Badruddin IA, et al. Pressure-driven electro-osmotic flow and mass transport in constricted mixing micro-channels. *Journal of Applied Fluid Mechanics* 2019; 13(2): 429–441. doi: 10.29252/jafm.13.02.30146
- Reddy KV, Makinde OD, Reddy MD. Thermal analysis of MHD electro-osmotic peristaltic pumping of Casson fluid through a rotating asymmetric microchannel. *Indian Journal of Physics* 2018; 92(11): 1439–1448. doi: 10.1007/s12648-018-1209-1
- Kmiotek M, Kucab-Pietal A. Influence of slim obstacle geometry on the flow and heat transfer in microchannels. *Bulletin of the Polish Academy of Sciences. Technical Sciences* 2018; 66(2): 111–118. doi: 10.24425/119064
- Dewan A, Srivastava P. A review of heat transfer enhancement through flow disruption in a microchannel. *Journal of Thermal Science* 2015; 24(3): 203–214. doi: 10.1007/s11630-015-0775-1
- Kumar R, Islam M, Hasan MM. A review of experimental investigations on heat transfer characteristics of single phase liquid flow in microchannels. *International Journal of Advanced Mechanical Engineering* 2014; 4(1): 115–120.
- Choi SUS, Eastman JA. Enhancing thermal conductivity of fluids with nanoparticles. *ASME International Mechanical Engineering Congress & Exposition* 1995; 66: 99–105.
- Subramanian KRV, Rao TN, Balakrishnan A. *Nanofluids and Their Engineering Applications*. CRC Press; 2020.
- Reddy KV, Reddy MG, Makinde OD. Thermophoresis and brownian motion effects on magnetohydrodynamics electro-osmotic jeffrey nanofluid peristaltic flow in asymmetric rotating microchannel. *Journal of Nanofluids* 2019; 8(2): 349–358. doi: 10.1166/jon.2019.1581
- Niazi MDK, Xu H. Modelling two-layer nanofluid flow in a microchannel with electro-osmotic effects by means of the Buongiorno's model. *Applied Mathematics and Mechanics* 2020; 41(1): 83–104. doi: 10.1007/s10483-020-2558-7

13. Ahadi A, Antoun S, Saghir MZ, Swift J. Computational fluid dynamic evaluation of heat transfer enhancement in microchannel solar collectors sustained by alumina nanofluid. *Energy Storage* 2019; 1(2): e37. doi: 10.1002/est2.37
14. Delisle CS, Welsford CA, Saghir MZ. Forced convection study with microporous channels and nanofluid: Experimental and numerical. *Journal of Thermal Analysis and Calorimetry* 2019; 140(6): 1205–1214. doi: 10.1007/s10973-019-09175-8
15. Sharaf OZ, Al-Khateeb AN, Kyritsis DC, Abu-Nada E. Numerical investigation of nanofluid particle migration and convective heat transfer in microchannels using an Eulerian-Lagrangian approach. *Journal of Fluid Mechanics* 2019; 878: 62–97. doi: 10.1017/jfm.2019.606
16. Shahrestani MI, Maleki A, Shadloo MS, Tlili I. Numerical investigation of forced convective heat transfer and performance evaluation criterion of  $Al_2O_3$ /water nanofluid flow inside an axisymmetric microchannel. *Symmetry* 2020; 12(1): 120. doi: 10.3390/sym12010120
17. Davood T, Mohammad M, Omid Ali A, et al. The effect of using water/CuO nanofluid and L-shaped porous ribs on the performance evaluation criterion of microchannels. *Journal of Thermal Analysis and Calorimetry* 2018; 135(4): 145–159. doi: 10.1007/s10973-018-7254-3
18. Pouya B, Davood T, Reza BD, Masoud A. Two phase natural convection and thermal radiation of Non-Newtonian nanofluid in a porous cavity considering inclined cavity and size of inside cylinders. *International Communications in Heat and Mass Transfer* 2019; 108: 104285. doi: 10.1016/j.icheatmasstransfer.2019.104285
19. Chamkha AJ, Azzi A, Menni Y. Transport of nanofluid through porous media—A review. *Special Topics & Reviews in Porous Media: An International Journal* 2018; 9(4): 1–16. doi: 10.1615/SpecialTopicsRevPorousMedia.2018027168
20. Chamkha AJ, Ameer H, Menni Y. Nanofluids advances through heat exchangers. *Heat Transfer* 2020; 1–29. doi: 10.1002/htj.2182
21. Algehyne EA, Wakif A, Rasool G, et al. Significance of Darcy-Forchheimer and Lorentz forces on radiative alumina-water nanofluid flows over a slippery curved geometry under multiple convective constraints: A renovated Buongiorno's model with validated thermophysical correlations. *Waves in Random and Complex Media* 2022. doi: 10.1080/17455030.2022.2074570
22. Rashad, AM, Chamkha AJ, Mansour MA, Armaghani T. MHD combined convection flow of Cu-water nanofluid through a lid-driven saturated porous enclosure with entropy generation and partial slip effects. *Journal of Thermal Analysis and Calorimetry* 2019; 132: 1291–1306. doi: 10.1007/s10973-018-7889-0
23. Maneengam A, Laidoudi H, Abderrahmane A, et al. Entropy generation in 2D lid-driven porous container with the presence of obstacles of different shapes and under the influences of buoyancy and lorentz forces. *Nanomaterials* 2022; 12(13): 2206. doi: 10.3390/nano12132206
24. Rasool G, Shah NA, El-Zahar ER, Wakif A. Numerical investigation of EMHD nanofluid flows over a convectively heated Riga pattern positioned horizontally in a Darcy-Forchheimer porous medium: Application of passive control strategy and generalized transfer laws. *Waves in Random and Complex Media* 2022. doi: 10.1080/17455030.2022.2074571
25. Makinde OD, Lakshmi DV, Venkateswarlu M. Heat generation and thermal radiation influences on the steady hydromagnetic flow through a vertical micro-porouschannel with suction/injection. *Journal of Nanofluids* 2019; 8(5): 1–10. doi: 10.1166/jon.2019.1647
26. Joshi N, Pandey AK, Upreti H, Kumar M. Mixed convection flow of magnetic hybrid nanofluid over a bidirectional porous surface with internal heat generation and a higher-order chemical reaction. *Heat Transfer* 2020; 50(4): 3661–3682. doi: 10.1002/htj.22046
27. Raza J, Mebarek-Oudina F, Ali Lund L. The flow of magnetised convective Casson liquid via a porous channel with shrinking and stationary walls. *Pramana* 2022; 96: 229. doi: 10.1007/s12043-022-02465-1
28. Mahmoud J, Ali Rabienataj DA, Davood T, Omidali A. Melting process in porous media around two hot cylinders: Numerical study using the lattice Boltzmann method. *Physica A: Statistical Mechanics and its Applications* 2018; 509: 316–335. doi: 10.1016/j.physa.2018.06.011
29. Arasteh H, Mashayekhi R, Toghraie D, et al. Optimal arrangements of a heat sink partially filled with multilayered porous media employing hybrid nanofluid. *Journal of Thermal Analysis and Calorimetry* 2019; 137(3): 1045–1058. doi: 10.1007/s10973-019-08007-z
30. Arasteh H, Mashayekhi R, Ghaneifar M, et al. Heat transfer enhancement in a counter-flow sinusoidal parallel-plate heat exchanger partially filled with porous media using metal foam in the channels' divergent sections. *Journal of Thermal Analysis and Calorimetry* 2019; 141(5): 1669–1685. doi: 10.1007/s10973-019-08870-w
31. Mehmood R, Nayak MK, Akbar NS, Makinde OD. Effects of thermal-diffusion and diffusion-thermoconvection oblique stagnation point flow of couple stress Casson fluid over a stretched horizontal riga plate with higher order chemical reaction. *Journal of Nanofluids* 2019; 8(1): 94–102. doi: 10.1166/jon.2019.1560

32. Thammanna GT, Kumar KG, Gireesha BJ, et al. Magnetohydrodynamic analysis on stretched flow of couple stress Casson fluid with chemical reaction. *Results in Physics* 2017; 7: 4104–4124. doi: 10.1016/j.rinp.2017.10.016
33. Mahanthesh B, Makinde OD, Gireesha BJ, et al. Two-phase flow of dusty Casson fluid with Cattaneo-Christov heat flux and heat source past a cone, wedge and plate. *Defect and Diffusion Forum* 2018; 387: 625–639. doi: 10.4028/www.scientific.net/DDF.387.625
34. Jakeer S, Reddy PBA, Reddy SRR, Basha HT. Entropy generation and Melting heat transfer on the Ferrohydrodynamic flow of  $Fe_3O_4$ -Ag/ blood hybrid nanofluid with Cattaneo-Christov heat flux model. *Waves in Random and Complex Media* 2023; 1–24. doi: 10.1080/17455030.2022.2164808
35. Patil MB, Shobha KC, Bhattacharyya S, Said Z. Soret and Dufour effects in the flow of Casson nanofluid in a vertical channel with thermal radiation: Entropy analysis. *Journal of Thermal Analysis and Calorimetry* 2023; 148(3): 1–11. doi: 10.1007/s10973-023-11962-3
36. Casson N. A flow equation for pigment-oil suspensions of the printing ink type. In: Mill CC (editor). *Rheology of Disperse Systems*. Pergamon Press; 1959. pp. 84–104.
37. Cebeci T, Bradshaw P. *Physical and Computational Aspects of Convective Heat Transfer*. Springer New York; 1984.
38. Roja A, Gireesha BJ, Nagaraja B. Irreversibility investigation of Casson fluid flow in an inclined channel subject to a Darcy-Forchheimer porous medium: A numerical study. *Applied Mathematics and Mechanics* 2021; 42: 95–108. doi: 10.1007/s10483-021-2681-9
39. Mahmoudi Y, Hooman K, Vafai K. *Convective Heat Transfer in Porous Media*. CRC Press; 2020.
40. Rundora L, Makinde OD. Buoyance effects on unsteady reactive variable properties fluid flow in a channel filled with a porous medium. *Journal of Porous Media* 2018; 21(8): 721–737. doi: 10.1615/JPorMedia.2018015707
41. Makinde OD, Khan ZH, Ahmad R, et al. Unsteady MHD flow in a porous channel with thermal radiation and heat source/sink. *International Journal of Applied and Computational Mathematics* 2019; 5: 59. doi: 10.1007/s40819-019-0644-9
42. Kasaeian A, Daneshazarian R, Mahian O, et al. Nanofluid flow and heat transfer in porous media: A review of the latest developments. *International Journal of Heat and Mass Transfer* 2017; 107: 778–791. doi: 10.1016/j.ijheatmasstransfer.2016.11.074
43. Menni Y, Chamkha AJ, Azzi A. Nanofluid transport in porous media: A review. *Special Topics & Reviews in Porous Media: An International Journal* 2019; 10(1): 49–64. doi: 10.1615/SpecialTopicsRevPorousMedia.2018027168
44. Nayak MK, Pandey VS, Shaw S, et al. Thermo-fluidic significance of non-Newtonian fluid with hybrid nanostructures. *Case Studies in Thermal Engineering* 2021; 26: 101092. doi: 10.1016/j.csite.2021.101092